

**This version of this paper is non-peer-reviewed and under review in Nature Geoscience**

This paper has been submitted for publication to Nature Geoscience on June 8 2020  
A revised version of this paper has been submitted on December 15 2020 and is under review.

Any comment can be sent to the corresponding author: [feuillet@ipgp.fr](mailto:feuillet@ipgp.fr)

1 **Birth of a large volcanic edifice through lithosphere-scale dyking offshore**  
2 **Mayotte (Indian Ocean)**

3  
4 N. Feuillet<sup>1,\*</sup>, S.J. Jorry<sup>2</sup>, W. Crawford<sup>1</sup>, C. Deplus<sup>1</sup>, I. Thinon<sup>3</sup>, E. Jacques<sup>1</sup>, J.M. Saurel<sup>1</sup>, A.  
5 Lemoine<sup>3</sup>, F. Paquet<sup>3</sup>, C. Satriano<sup>1</sup>, C. Aiken<sup>2</sup>, O. Foix<sup>1</sup>, P. Kowalski<sup>1</sup>, A. Laurent<sup>1</sup>, E.  
6 Rinnert<sup>2</sup>, C. Cathalot<sup>2</sup>, J.P. Donval<sup>2</sup>, V. Guyader<sup>2</sup>, A. Gaillot<sup>2</sup>, C. Scalabrin<sup>2</sup>, M. Moreira<sup>1</sup>, A.  
7 Peltier<sup>1</sup>, F. Beauducel<sup>1,4</sup>, R. Grandin<sup>1</sup>, V. Ballu<sup>5</sup>, R. Daniel<sup>1</sup>, P. Pelleau<sup>2</sup>, J. Gomez<sup>1</sup>, S.  
8 Besançon<sup>1</sup>, L. Geli<sup>2</sup>, P. Bernard<sup>1</sup>, P. Bachelery<sup>6</sup>, Y. Fouquet<sup>2</sup>, D. Bertil<sup>3</sup>, A. Lemarchand<sup>1</sup>, J.  
9 Van der Woerd<sup>7</sup>.

10  
11 1- Université de Paris, Institut de physique du globe de Paris, CNRS, F-75005 Paris,  
12 France

13 2- IFREMER, Unité Géosciences Marines, Technopole La Pointe du Diable, 29280  
14 Plouzané, France

15 3- Bureau de Recherches Géologiques et Minières - BRGM, DGR/GBS, F-45060  
16 Orléans, France

17 4- Université Grenoble Alpes, IRD, ISterre

18 5- Littoral ENvironnement et Sociétés (LIENSs) UMR7266, Université de La Rochelle -  
19 CNRS, 2 rue Olympe de Gouges, 17000 La Rochelle

20 6- Université Clermont Auvergne, CNRS, IRD, OPGC, Laboratoire Magmas et Volcans,  
21 F-63000 Clermont-Ferrand, France,

22 7- Institut de Physique du Globe de Strasbourg UMR7516 CNRS Université de  
23 Strasbourg, 5 rue René Descartes 67000 Strasbourg, France

24  
25  
26  
27  
28 **Volcanic eruptions are foundational events that shape the Earth's surface and provide a**  
29 **window into deep Earth processes. How the primary asthenospheric melts form, pond**  
30 **and ascend through the lithosphere is, however, still poorly understood. We document**  
31 **an on-going magmatic event offshore Mayotte Island (North Mozambique channel),**  
32 **associated with large surface displacements, very low frequency earthquakes and**  
33 **exceptionally deep (25-50 km) seismicity swarms. We present data from the May 2019**  
34 **MAYOBS1 cruise, which reveal that this event gave birth to a 820m tall, ~ 5 km<sup>3</sup> deep-**  
35 **sea volcanic edifice. This is the largest active submarine eruption ever documented. The**  
36 **data indicate that deep magma reservoirs were rapidly drained through dykes that**  
37 **intruded the entire lithosphere and that pre-existing subvertical faults in the mantle**  
38 **were reactivated beneath an ancient caldera structure.**

39

40

41 **The new volcanic edifice is located at the tip of a 50 km-long volcanic ridge on the**  
42 **eastern insular slopes of Mayotte. The ridge is composed of many other recent edifices**  
43 **and lava flows and is an extensional feature that opens inside a wide transtensional**  
44 **boundary to transfer the strain between the East-African and Madagascar rifts. A hot**  
45 **asthenosphere at the base of a thick damaged lithosphere could be at the origin of this**  
46 **massive eruption.**

47

48 Since May 10 2018, Mayotte Island (Comoros archipelago, north Mozambique Channel  
49 between Africa and Madagascar, *Figure 1a*) has experienced a major magmatic event off its  
50 eastern coast. This event generated more than 11000 detectable earthquakes (up to Mw 5.9),  
51 surface deformation rates of up to 200 mm/year and unusual very low frequency (VLF)  
52 earthquakes<sup>1,2,3</sup>. As of December 2020 (the time of writing), Mayotte is still deforming and  
53 both VLF events and earthquakes with Mw up to 5 are still being recorded.

54 Prior to this event, no recent eruption or significant seismic activity was reported around  
55 Mayotte. Only two earthquakes were detected within 100 km of the island by the global  
56 network since 1972<sup>4</sup> and the most recent volcanic exposure is a 4-6 kyr-old pumice layer  
57 sampled in the lagoon surrounding the island<sup>5</sup>.

58 Recent geodynamic reconstructions suggest that the archipelago was built on ~150 Ma old  
59 oceanic lithosphere accreted to accommodate the opening of the Western Somali Basin<sup>6</sup>. This  
60 Comorian volcanism may result from partial melting of the base of this old oceanic  
61 lithosphere in interaction with plume material<sup>7,8,9</sup> possibly super plumes originating from  
62 Africa<sup>10,11,12</sup>. This volcanism may have been controlled by reactivation of the fractures zones<sup>13</sup>  
63 or by diffuse zones of right-lateral shear deformation<sup>14</sup>. Subaerial volcanic activity on Mayotte

64 island began 11 My ago<sup>13</sup>. Well-preserved cones, tuff rings and maar craters in the  
65 Northeastern part of the island (on Petite Terre and in and around Mamoudzou<sup>15,7</sup> and further  
66 offshore<sup>16</sup> (*Figure 1b*) testify to relatively recent (probably Holocene<sup>7</sup>) subaerial explosive  
67 volcanic activity. Gas emissions on Petite-Terre with a high percentage of carbon dioxide and  
68 helium indicate magma degassing<sup>17</sup>.

69

## 70 **The discovery of the new volcanic edifice**

71 The French national research program “SISMAYOTTE” was launched in February 2019 to  
72 determine the origin of the seismicity and deformation, to search for any seafloor volcanic  
73 activity and to understand the scale, chronology and implications of the crisis. As part of this  
74 program, we 1) set up seismic and Global Navigation Satellite System (GNSS) stations on  
75 Mayotte and Grande Glorieuses Islands, 2) deployed Ocean Bottom Seismometers (OBS)  
76 with attached Absolute Pressure Gauges (APG) around the seismic swarm area, and 3)  
77 acquired high-resolution marine data (bathymetry, seafloor and water column backscatter,  
78 sub-bottom, magnetic and gravity profiles), rock dredges and CTD (Conductivity-  
79 Temperature-Depth)- Rosette during the MAYOBS1 cruise aboard the R/V Marion  
80 Dufresne<sup>18</sup>.

81 A systematic 12 kHz multibeam echosounder survey east of Mayotte revealed a 820 m tall  
82 new volcanic edifice (NVE) 50 km east of Mayotte (*Figure 1*). The NVE was detected by  
83 comparing our data to those acquired during a 2014 survey by the French Naval Hydrographic  
84 and Oceanographic Service (SHOM)<sup>19</sup> (*Figure 2a*). The edifice sits on an area that, in the  
85 2014 seafloor topography, was locally almost flat at around 3300 m below sea level (bsl).

## 86 **The Mayotte volcanic ridge**

87 The NVE has grown on the lower insular slope of Mayotte, near the end of a WNW-ESE  
88 trending volcanic ridge (Mayotte ridge) emplaced on the submarine flank of Mayotte (*Figure*

89 1). The NVE and many other volcanic features along the ridge are highly reflective in seafloor  
90 imagery (*Figure 1c and extended data Figures 1, 3*) indicating recent volcanic activity all  
91 along the ridge. The ridge is 50 km long, extending from the most recent subaerial cones and  
92 maar craters on Grande-Terre and Petite-Terre islands (MPT Volcanic zone) to the NVE  
93 (*Figure 1b*). It is segmented into two main parts: an upper slope volcanic zone (western  
94 segment) and a mid- to lower-slope zone (eastern segment). The eastern segment trends  
95 N130°E and is made of many constructional features similar to mafic submarine eruption  
96 features observed elsewhere <sup>20,21,22</sup>: cones up to 2 km-wide and 500 m-high, probably  
97 monogenetic; high backscatter zones with smooth bathymetry, which could correspond to  
98 recent lava flows; elongated ridges with steep slopes and varying orientations, which could  
99 result from dykes in more sedimented areas (*Figure 1 and extended data Figure 2d,e*).

100 The western segment is made of volcanic features having more complex morphologies and  
101 emplaced along different directions (*Figure 1b and extended data Figure 2b,c*). The main  
102 features are: i) Two N40°E and N120°E trending sets of cones and lava flows, with high  
103 backscatter, northeast and southeast of Petite-Terre, respectively. These sets converge to  
104 prolong the onshore maar craters of Petite-Terre and may have emplaced along pre-existing  
105 fractures or faults; ii) a horse-shoe shaped edifice (the Horseshoe) with a 3.5 km wide cone,  
106 steep slopes and a large collapse-induced scar. East of the Horseshoe, several smaller cones  
107 and volcanic features are aligned E-W, suggesting eruptive fissures. Large lava flows  
108 characterized by high backscatter and rough bathymetry likely originate from this fissure  
109 system. iii) a 4 km-wide circular structure (the Crown), whose rim is crowned by seven 1 km-  
110 wide, 100-150m high volcanic cones. Their arrangement suggests typical post-caldera domes  
111 <sup>23,24</sup>. West of the Crown, submarine canyons and slope failure scars all terminate at a N-S  
112 trending slope break that may be controlled by faulting. The Crown appears to be located in a

113 larger 10 km wide flat depression, which is bounded by faults and fissures and could be the  
114 remnant of an ancient caldera collapse.

### 115 **The new volcanic edifice and the eruptive plume**

116 The NVE is located at the eastern tip of the eastern segment of the Mayotte ridge (*Figures*  
117 *1b*). In May 2019, its summit rose to 2580 m bsl. The highest and central part of the NVE  
118 resembles a pyramid with steep and smooth slopes (*Figure 2a and extended data Figure 3*).

119 Radial ridges, up to 5 km long and 300 m thick, develop from the central part. The ridges  
120 display hummocky morphology similar to that observed along mid-ocean volcanic ridges<sup>25</sup>  
121 and active seamounts<sup>22</sup> and probably correspond to coalesced pillow lava mounds<sup>21</sup>. Beyond  
122 and in-between the hummocky ridges, flat areas up to 100 m thick, with high backscatter,  
123 could indicate channelized lava flows or sheet flows emplaced at high effusion rates<sup>26,27</sup>. We  
124 calculate the volume of material corresponding to the 2014- 2019 seafloor depth difference to  
125 be at least  $5.0 \pm 0.3 \text{ km}^3$ . Popping fragments of very fresh basanitic pillow lavas (SiO<sub>2</sub> 47  
126 wt%, Na<sub>2</sub>O + K<sub>2</sub>O 7.1 wt%, MgO 5.7 wt%<sup>28</sup>) were dredged on the northeastern flank of the  
127 NVE, near its summit (see *Figure 2a* for sample location and *supplementary material SI*).  
128 The lavas, similar to other basanites sampled in northern Mayotte<sup>7</sup> are aphyric with rare  
129 microphenocrysts of olivine (Fo70) and Ti-magnetite.

130 A ~1900-m high, vertical acoustic plume, rising through the water column from the summit of  
131 the NVE to ~800 m below the sea surface, was imaged several times during the cruise using  
132 the ship-borne multibeam echosounder (*Figure 3*, supplementary movie 1). A vertical  
133 CTD/rosette cast to 3137m depth above the northern flank of the NVE, 1000m away from the  
134 acoustic plume, showed strong geochemical signatures. High volatile concentrations (H<sub>2</sub> =  
135 550nM, CH<sub>4</sub> = 831 nM, CO<sub>2</sub>= 34 μM), high turbidity and high total alkalinity values were  
136 associated with temperature and pH anomalies (respectively 0.2°C and 1 pH unit)<sup>29</sup> and  
137 *supplementary material*). Such chemical anomalies are characteristic of submarine eruptions

138 and may reflect magma degassing <sup>30</sup>, molten lava interaction with seawater <sup>31</sup> or fluid/water  
139 discharge from subsurface storage zones in the crust or sedimentary cover <sup>32</sup>. The height and  
140 the strong backscatter signature of the acoustic plume suggest that a mixture of solid particles  
141 (pyroclastic/hyaloclastic jet <sup>30</sup>) and/or differentiated fluid phases (droplets, hydrate-coated  
142 bubbles or free gas <sup>33</sup>) are driven upward through the water column from the summit of the  
143 NVE <sup>34</sup>. High turbidity measured, below 2500 m, on the northern flank of the NVE, likely  
144 indicates the presence of these particles <sup>35,36</sup>. Both the multiple observations of this vertical  
145 acoustic plume at the summit of the NVE and the high H<sub>2</sub> concentration 1 km away indicate  
146 that the eruption was likely on-going in May 2019 <sup>31</sup>.

147 In the upper slope zone, 30 km far from the volcano, two, ~1000-m high acoustic plumes  
148 were detected in the water column, above the Horseshoe edifice (*Figure 1 and extended data*  
149 *Figure 5, movie 2*) but no significant change in the seafloor morphology and reflectivity was  
150 detected there.

151

## 152 **The seismicity and VLF events relocated by OBS data**

153 The combined land-OBS network of seismic stations (*supplement Figure S2.1*) detected  
154 17000 events between February 25 and May 6, 2019. We manually relocated about 800 of the  
155 largest earthquakes onboard (*see method and supplementary S2*). Ninety-four percent of the  
156 earthquakes cluster in the upper slope volcanic zone (western segment of the Mayotte ridge),  
157 40 km west of the NVE and 5 to 15 km east of Petite-Terre (swarm 1, *Figure 1*). Almost all of  
158 the remaining events lie in a secondary swarm beneath the northwestern tip of the eastern  
159 segment, 30 km from Petite-Terre and 20 km from the NVE (swarm 2, *Figure 1*). A few  
160 events are also scattered along this segment. Despite a full search of the OBS-land catalog for  
161 events beneath the NVE, we found none. The earthquakes are very deep, ranging from 25±5  
162 to 50±5 km. All P-S arrival delays recorded by an OBS deployed for 48h above the main

163 swarm were greater than 3 seconds, indicating no events less than 20 km depth (*Figure 4,*  
164 *extended data Figure 6b, method and supplementary material S2*). The combined land-OBS  
165 network dataset do not show any evidence for seismicity migration, but it only represents a  
166 two-month “snapshot” of the activity. To extend the observation time window, we carefully  
167 relocated 139 earthquakes recorded by the land stations between the beginning of the crisis  
168 (May 2018) and the first OBS deployment (February 2019). All the events were beneath the  
169 volcanic ridge (*extended data figure 6a*). During the first weeks of the crisis, these events  
170 were mainly located beneath the northwestern tip of eastern ridge segment between 30 and 50  
171 km depth. In the last two weeks of June, a few events occurred between 30km-depth and the  
172 surface, and closer to the NVE.

173 In addition to the high frequency seismicity, VLF events were recorded by the OBSs  
174 wideband hydrophones. Their waveforms are similar to those of the globally detected  
175 November 11 2018 event (exponentially decaying monochromatic signals of approximately  
176 2000s duration, with dominant period of  $\sim 15$  s and polarized Rayleigh waves), suggesting  
177 repeated excitation of the same radiating source. We located 84 VLF events using waveform  
178 cross-correlation (*see method and supplementary material S2*), all of them are most probably  
179 above seismic swarm 1 (*Figures 4 and extended data Figure 6b*), at a mean depth of  $22 \pm 15$   
180 km.

181

## 182 **GNSS data and APG modeling**

183 The GNSS network includes nine stations on Mayotte Island and two far field stations at  
184 Diego Suarez and Grande Glorieuse islands. The geometry is not optimal, preventing geodetic  
185 inversions for complicated structures or media. We performed Bayesian inversions<sup>37</sup> of the  
186 data using a point source in an elastic half-space with two distinct analytical formalisms: an  
187 isotropic point source<sup>38</sup> and a point compound dislocation model (pCDM<sup>39</sup> *see method,*

188 *supplementary material S3, extended data Figure 7*). In both cases, the results indicate  $\sim 5 \text{ km}^3$   
189 deflation of a deep reservoir ( $> 30 \text{ km}$ ). The simplest and most robust model indicates the  
190 deflation of  $\sim 40 \text{ km}$  deep isotropic source below the eastern segment of the Mayotte ridge.  
191 An increase in absolute seafloor pressure measured by all APGs on the OBS frames,  
192 interpreted as seafloor subsidence, is compatible with these models (*see method,*  
193 *supplementary S3, extended data Figure 7d*).

194

### 195 **Magma reservoirs and chronology of the eruption**

196 Most of the seismicity and the GNSS sources models are deep and lie in the lithospheric  
197 mantle beneath the Moho, which is estimated to be  $\sim 17 \text{ km}$  deep beneath Mayotte <sup>40</sup>.  
198 Seismicity this deep is rarely documented in a volcanic context, especially in the form of  
199 dense swarms during eruptions. Mantle seismicity has been detected beneath Kilauea, Loihi <sup>41-</sup>  
200 <sup>43</sup> and La Réunion <sup>44</sup> volcanoes, where it has been interpreted as failure of the brittle  
201 lithosphere induced by magma migration through long-lived tectonic structures or by the  
202 islands' loading.

203 The distribution of the seismicity in the first weeks of the crisis suggests a dyke migration  
204 from the mid-slope zone to the NVE, along the eastern segment of the Mayotte ridge. This is  
205 supported by the migration of the Centroid Moment Tensor solutions depths (CMT project) of  
206 the largest earthquakes towards the surface (*extended data Figures 6c and 8*) and agrees well  
207 with <sup>45,2</sup>. The earthquakes show strike-slip focal mechanisms compatible with a least  
208 compressive principal stress orthogonal to the eastern segment of the ridge (*extended data*  
209 *Figure 8*). Similar stress trends have been observed during dyking events beneath the Izu  
210 peninsula in Japan <sup>46,47</sup> and in Iceland <sup>48</sup> but at much shallower depths, where they were  
211 interpreted as seismic shear faulting caused by stress transfer to the surrounding vertical faults  
212 in response to dyke opening and propagation <sup>46,47,48,49</sup>.

213 During the first six weeks of the crisis, the magma migrated 20 km laterally along the eastern  
214 segment of the Mayotte ridge, then upward (*Figure 4 and extended data Figure 8*). The  
215 building of the NVE may have begun in July 2018 once the dyke reached close to the surface  
216 <sup>2,1</sup> allowing for high magma flow rates and rapid ensuing growth. On the basis of this  
217 assumption, we estimate a minimum mean lava flow rate of  $\sim 180\text{m}^3\text{s}^{-1}$  between the start of  
218 the eruption on the seafloor and our survey ( $\sim 11$  months). The local stress probably  
219 decreased considerably once the magma path to the NVE was opened, as is observed during  
220 many eruptions involving dyke propagation <sup>50</sup>, which would explain why no earthquakes were  
221 detected beneath the NVE during the OBS deployment, which started in late February 2019.  
222 After the dike reached the near surface, seismicity resumed beneath the mid- and upper-slope  
223 volcanic zones (*Figure 4 and extended data Figures 6a,b and 8*) and its pattern appears to be  
224 constant since September 2018 <sup>2</sup>. This stationary seismicity could be caused by stress  
225 perturbation along pre-existing structures and/or fluid (gas, magma or water) motions. The  
226 swarm 1 earthquakes cluster beneath a 10 km-wide circular area that coincides with the  
227 ancient caldera structure inferred from our high-resolution bathymetry (*Figure 1c and*  
228 *extended data Figure 6b and 8*). This seismicity could indicate activation of pre-existing  
229 subvertical faults <sup>51</sup> above a deep ( $> 55$  km) depleting reservoir (R1,4), as has been observed  
230 during caldera collapse events <sup>52,53,54</sup> but these faults would be much deeper than at any caldera  
231 structures documented elsewhere. Analog models for collapse of a caldera with a high-roof  
232 aspect ratio (thickness/width  $\gg 1$ ) indicate reverse fault motions during an initial downsag  
233 stage <sup>55</sup>, in accord with the focal mechanism of the May 14, 2019 Mw4.9 swarm 1 region  
234 earthquake (*Figure 4 and extended data Figure 8*) and <sup>45</sup>.

235 The VLF events, located above swarm1, may be generated by the resonance of a fluid-filled  
236 (magma, gas or hydrothermal) shallower cavity or a fluid-filled crack, most probably at the  
237 base of the crust. The characteristic frequency and duration of these events are very different

238 from VLF events typically observed in volcanic zones <sup>56,57,58,59,60,61</sup>. Simple up-scaling of fluid  
239 resonance models <sup>62,63</sup> imply a size of several kilometres for this shallower reservoir (R3,  
240 *Figure 4*). The excitation mechanism could be rapid slip and related strain on faults close to  
241 the reservoir or episodic collapse of a piston at the base of this shallow reservoir <sup>64</sup>. The  
242 acoustic plumes emanating from the overlying Horseshoe edifice may result from actively  
243 degassing of this shallower reservoir.

244 Both the distribution of seismicity over time and the surface deformation models suggest the  
245 drainage of an exceptionally deep reservoir by a dyke that propagated from the base of the  
246 brittle lithosphere to the eastern portion of the Mayotte ridge, possibly intersecting another  
247 vertical storage zone below seismic swarm 2 before reaching the surface (*R2, Figure 4 and*  
248 *extended data Figure 9*). Within the uncertainties the GNSS isotropic model may reflect the  
249 drainage of this reservoir R2 in the brittle lithosphere. The deeper reservoir R1 may have  
250 slowly recharged from the asthenosphere before reaching tensile failure in May 2018 <sup>65</sup>.

### 251 **Magma roots and paths.**

252 The eastern segment of the Mayotte ridge, along which the dike propagated, has the same  
253 orientation as many other volcanic features over a range of scales (quaternary dykes, volcanic  
254 vent alignments, ridges and volcanic rift zones) in the northeastern part of Mayotte Island <sup>15</sup>  
255 and in and around the other Comoros islands <sup>13,66,14</sup> (*Figure 5 and extended data Figure 9*). The  
256 left-lateral en-echelon arrangement of these features resembles that of extensional tectonic  
257 structures in a context of oblique extension (i.e in segmented and diffuse strike-slip fault  
258 systems <sup>67</sup> or highly-oblique rifting <sup>68, 69,70,71</sup>). We infer that the Mayotte ridge results from the  
259 interplay between volcanism and tectonics. The location and orientation of the volcanic  
260 features may be in part controlled by the pre-existing Mesozoic fracture zones <sup>6</sup> but they  
261 probably also emplace along new tectonic structures. These tectonic structures are extensional  
262 (fissures or step-overs) and open as a result of volcano-tectonic interactions in a wide E-W

263 striking zone, to transfer the strain between the N-S striking offshore branches of the East  
264 African rift <sup>72</sup> and the grabens of Madagascar (Aloatra and Ankai) <sup>73,74</sup>. In this context, high  
265 strain rates <sup>69</sup> or highly damaged zones may develop <sup>75</sup> (*Figure 5a inset*) in between the main  
266 en-echelon extensional structures. Such zones may constitute high-permeability zones where  
267 large magmatic reservoirs can develop. The main Comoros volcanic islands may have grown  
268 above such zones.

269 Between Mayotte and Madagascar, the lithosphere-asthenosphere boundary (LAB) is a sharp  
270 limit between a high-velocity 150 Ma lithosphere and a low-velocity asthenosphere, at about  
271 70 km depth <sup>76,77</sup>. The low-velocity asthenosphere is interpreted as hot material spreading  
272 beneath the Mascarene basin and beyond <sup>78</sup>. Heating of the base of the oceanic  
273 lithosphere damaged by extensional tectonic and loaded by Mayotte island <sup>79</sup> may favour the  
274 ponding and withdrawal of large volumes of buoyant melts. Pore pressure increase in these  
275 zones may in turn favour failure of deep reservoirs and faults inside the brittle lithosphere

### 276 **The largest eruption ever documented in submarine domain**

277 The NVE extruded volume (as of May 2019) is 30 to 1000 times larger than that reported for  
278 other deep-sea eruptions <sup>21,26,27,80,81</sup>. As is the case for many submarine eruptions, it is difficult  
279 to evaluate the dense rock equivalent (DRE) volume <sup>20</sup>. Taking an upper bound of 50% for the  
280 DRE factor <sup>82</sup>, compatible with the 40% vesicularity of our sample <sup>28</sup>, the DRE erupted  
281 volume could be as large as 2.5 km<sup>3</sup>, which is larger than the 1.2 to 1.5 km<sup>3</sup> Havre silicic  
282 eruption <sup>83,84</sup>, up to now considered to be the largest documented submarine eruption. It would  
283 be 2.5 times larger than the Bardabunga eruption (Iceland's largest eruption of the last two  
284 centuries) <sup>50,85</sup> and only 6 times less than Iceland's 1783-1784 Laki eruption, considered to be  
285 one of the largest basaltic eruptions witnessed by humanity <sup>86</sup>. The volumes and flux of  
286 emitted lava during the Mayotte magmatic event are comparable to those observed during  
287 eruptions at Earth's largest hot spots (Hawaii, Iceland, <sup>50,87</sup> and one quarter of that emplaced

288 yearly over the entire mid-ocean ridge system (mean estimate from spreading rates over the  
289 last 80 Ma <sup>88</sup>). It thus represents a considerable input in terms of CO<sub>2</sub> flux <sup>89</sup>.

290 Future scenarios could include a new caldera collapse, submarine eruptions on the upper  
291 slope, or onshore eruptions. Large lava flows and cones on the upper slope and onshore  
292 Mayotte indicate that this has occurred in the past. Since the discovery of the NVE, an  
293 observatory has been established to monitor activity in real time (REVOSIMA <sup>90</sup>) and return  
294 cruises are ongoing to follow the evolution of the eruption and edifices.

295

## 296 **Acknowledgements**

297 We thank captain A. Eyssautier and the officers and the crew of the R/V *Marion Dufresne*  
298 (TAAF/IFREMER/LDA), GENAVIR's coordinator, M. Boudou D'hautefeuille, and the  
299 shipboard operations engineers. We thank the captain and crew of the M/V *Ylang* (SGTM  
300 company). We thank the French Ministries of Environment, Research and Overseas,  
301 CNRS/INSU, IPGP, IFREMER, BRGM and the Prefect of Mayotte for funding and support.  
302 We thank our colleagues F. Tronel, A. Roulle, E. Dectot, A. Colombain, C. Doubre, Daniel  
303 Sauter, Antony Dofal and Antoine Villié for assistance in the field, previous data acquisition,  
304 processing and model development. We thank Olivier Desprez de Gesincourt, L. Testut and  
305 T. Tranchant for loan and data processing of the seafloor pressure sensors. We thank the  
306 French National Marine Hydrographic and Oceanographic Service (SHOM) for providing us  
307 with previous data from the area. We thank G. Barruol for discussions. This is IPGP  
308 contribution number XXXX.

309

## 310 **Method Summary**

311 **Ship-borne Multibeam data** was acquired using a Kongsberg EM122 1°x1° during the 2014  
312 <sup>19</sup> and 2019 <sup>18</sup> cruises. Both data sets were processed with the GLOBE software <sup>91</sup> to provide

313 30-m grid spaced digital terrain models and seafloor backscatter imagery and to calculate  
314 depth differences, surface and volumes. The 3D acoustic water column data from the 2019  
315 cruise were processed using SonarScope (@Ifremer) and GLOBE softwares <sup>91</sup>. **Water**  
316 **column measurements:** A CTD-Rosette Seabird 911+ CTD (Conductivity; Temperature;  
317 Depth) equipped with an altimeter, an Aanderaa oxygen optode and a Seapoint Turbidity  
318 Meter was mounted on a carousel with 16 Niskin sampling bottles (8L) to measure and  
319 sample throughout the water column. Sub-sampling was performed for onboard analyses  
320 (pH, alkalinity and total CO<sub>2</sub> by pH electrode and titrator) and for onshore analyses (CH<sub>4</sub>  
321 analysis by the purge and trap method and H<sub>2</sub> and CO<sub>2</sub> analysis by the Headspace method).  
322 **Seismology:** 800 earthquakes identified from the onshore catalog were selected in  
323 descending magnitude order and manually picked onboard. The seismic network used during  
324 the two month deployment included OBSs, onshore local and regional stations (up to 500km  
325 distance). The events were relocated with NonLinLoc <sup>92</sup> and an hybrid velocity model based  
326 on trials with 6 different velocity models, achieving final location accuracies better than 5km.  
327 Eighty-four very low frequency (VLF) earthquakes were detected between February 25 and  
328 April 24, 2019, using an amplitude trigger on ocean bottom hydrophones recordings, filtered  
329 between 0.05 and 0.10 Hz, followed by a selection of events with a clear peak frequency and  
330 a final visual inspection. VLF earthquakes were located using spatial 3D back-projection of  
331 station-pair cross-correlation functions <sup>93</sup>, assuming a constant surface-wave speed of 3.5  
332 km/s. A well-constrained epicentral location was obtained for 81 events. **Geodesy:** We  
333 inverted the surface deformation recorded by 6 permanent GNSS (Global Navigation Satellite  
334 System) receivers installed in Mayotte, Grande Glorieuse and Madagascar. We used both an  
335 isotropic model and a triple volumetric discontinuities (pCDM source) in a homogeneous  
336 elastic half-space, isotropic material with Poisson's ratio of 0.25 to model the pressure source  
337 in depth. Seafloor pressure data (30s sample interval) were pre-processed using harmonic

338 analysis to remove the tides and low-pass filtering to remove residual oscillations interpreted  
339 as internal waves.

#### 340 **Author contributions**

341 NF, SJ, WC, CD, IT, EJ, JMS, ALe, FP, RD, AG, CA, OF, PK, ALa, JPD, LG, JG, VG, PP,  
342 ER participated on the MAYOBS1 cruise (NF, SJ and WC as PI), acquired and processed the  
343 geophysical and seismological data. CSa, ALa and PB detected and located the VLF events.  
344 AP was in charge of the GNSS installation in Glorieuse island and processed and modeled the  
345 GNSS data with FB and RG. VB was in charge of the OBSs APGs and processed their data.  
346 SB participated in the first OBS deployment on the Ylang vessel with WC and RD. DB, ALM  
347 and JW were responsible for the installation of new seismological and GNSS stations in  
348 Mayotte and of data acquisition onshore. JPD, VG, ER, CC performed the geochemical  
349 analysis and interpretation of the water column data. CSc and AG processed the EM122  
350 acoustic data. CD and AG performed the depth changes calculation. CSc provided the  
351 interpretation of the water column acoustic data. PBa and YF furnished the rocks sample  
352 descriptions and petrological analysis. NF, SJ, CD, PBa, YF, IT, FP, JW, EJ provided the  
353 geological interpretation.. NF wrote the paper with the contribution of all other authors. JMS,  
354 EJ, CSa, ALe, GL, CA, VB, AG, AP, FB, RG, ER, CC, CSc wrote the supplementary method  
355 and method online.

#### 356 **Data availability statement**

357 The authors declare that most of the data supporting the findings of this study are available  
358 within the paper and its supplementary information files. GNSS data are available on the  
359 website « <http://mayotte.gnss.fr> ». Ship-borne geophysical data from the MAYOBS1 cruise  
360 can be obtained through the French national oceanographic data center SISMER  
361 (<http://en.data.ifremer.fr/SISMER>) but restrictions apply to the availability of these data. The

362 compilations of older bathymetric and topographic data are available on the SHOM Website  
363 (<http://www.shom.fr>)

## REFERENCES

- 1 Cesca, S. *et al.* Drainage of a deep magma reservoir near Mayotte inferred from seismicity and deformation. *Nat. Geosci.* **13**, 87-93, doi:10.1038/s41561-019-0505-5 (2020).
- 2 Lemoine, A., Bertil, D., Roullé, A. & Briole, P. The volcano-tectonic crisis of 2018 east of Mayotte, Comoros islands. *Geophys. J. Int.*
- 3 REVOSIMA, R. d. s. V. e. S. d. M. REVOSIMA (2020), Bulletin n°18 de l'activité sismo-volcanique à Mayotte, du 1 au 31 août, . Report No. 2680-1205, (2020).
- 4 U.S. Geological Survey. (<https://earthquake.usgs.gov/earthquakes/search> 2019).
- 5 Zinke, J., Reijmer, J. & Thomassin, B. Systems tracts sedimentology in the lagoon of Mayotte associated with the Holocene transgression. *Sedimentary Geology* **160**, 57-79 (2003).
- 6 Phethean, J. J. *et al.* Madagascar's escape from Africa: A high - resolution plate reconstruction for the Western Somali Basin and implications for supercontinent dispersal. *Geochemistry, Geophysics, Geosystems* **17**, 5036-5055 (2016).
- 7 Pelleter, A.-A. *et al.* Melilite-bearing lavas in Mayotte (France): An insight into the mantle source below the Comores. *Lithos* **208-209**, 281-297, doi:10.1016/j.lithos.2014.09.012 (2014).
- 8 Class, C., Goldstein, S. L., Altherr, R. & Bachèlery, P. The process of plume–lithosphere interactions in the ocean basins—the case of Grande Comore. *Journal of Petrology* **39**, 881-903 (1998).
- 9 Claude-Ivanaj, C., Bourdon, B. & Allègre, C. J. Ra–Th–Sr isotope systematics in Grande Comore Island: a case study of plume–lithosphere interaction. *Earth and Planetary Science Letters* **164**, 99-117 (1998).
- 10 Ebinger, C. J. & Sleep, N. Cenozoic magmatism throughout east Africa resulting from impact of a single plume. *Nature* **395**, 788-791 (1998).
- 11 Reiss, M., Long, M. & Creasy, N. Lowermost mantle anisotropy beneath Africa from differential SKS - SKKS shear - wave splitting. *Journal of Geophysical Research: Solid Earth* **124**, 8540-8564 (2019).
- 12 Class, C., Goldstein, S. L., Stute, M., Kurz, M. D. & Schlosser, P. Grand Comore Island: A well-constrained “low 3He/4He” mantle plume. *Earth and Planetary Science Letters* **233**, 391-409 (2005).
- 13 Nougier, J., Cantagrel, J. & Karche, J. The Comores archipelago in the western Indian Ocean: volcanology, geochronology and geodynamic setting. *J. Afr. Earth Sci.* (1983) **5**, 135-145 (1986).
- 14 Famin, V., Michon, L. & Bourhane, A. The Comoros archipelago: a right-lateral transform boundary between the Somalia and Lwandle plates. *Tectonophysics* **789**, 228539 (2020).
- 15 Nehlig, P. *et al.* Report French geological map (1/30 000), sheet Mayotte (1179). Orléans: BRGM, 74 p. . **Geological map by Lacquement F., Nehlig P., Bernard J. (2013).** (2013).
- 16 Audru, J.-C., Guennoc, P., Thinon, I. & Abellard, O. Bathymay : la structure sous-marine de Mayotte révélée par l'imagerie multifaisceaux. *Comptes Rendus Geoscience* **338**, 1240-1249, doi:10.1016/j.crte.2006.07.010 (2006).
- 17 Sanjuan, B. *et al.* Estimation du potentiel géothermique de Mayotte : Phase 2 - Étape 2. Investigations géologiques, géochimiques et géophysiques complémentaires, synthèse des résultats. 82 (BRGM, Orléans, France, 2008).
- 18 Feuillet, N. MAYOBS1 French Oceanographic cruise, RV Marion Dufresne. doi:<https://doi.org/10.17600/18001217> (2019).
- 19 SHOM. (2014).
- 20 Rubin, K. H. *et al.* Volcanic eruptions in the deep sea. *Oceanography* **25**, 142-157 (2012).
- 21 Chadwick Jr, W. W. *et al.* Recent eruptions between 2012-2018 discovered at West Mata submarine volcano (NE Lau Basin, SW Pacific) and characterized by new ship, AUV, and ROV data. *Frontiers in Marine Science* **6**, 495 (2019).
- 22 Clague, D. A. *et al.* Structure of Lō'ihi Seamount, Hawai'i, and Lava Flow Morphology from High-resolution Mapping. *Frontiers in Earth Science* **7**, 58 (2019).
- 23 Cole, J., Milner, D. & Spinks, K. Calderas and caldera structures: a review. *Earth-Science Reviews* **69**, 1-26 (2005).
- 24 Mauri, G., Williams-Jones, G., Saracco, G. & Zurek, J. M. A geochemical and geophysical investigation of the hydrothermal complex of Masaya volcano, Nicaragua. *Journal of Volcanology and Geothermal Research* **227**, 15-31 (2012).
- 25 Yeo, I. A. & Searle, R. High - resolution Remotely Operated Vehicle (ROV) mapping of a slow - spreading ridge: Mid - Atlantic Ridge 45° N. *Geochemistry, Geophysics, Geosystems* **14**, 1693-1702 (2013).
- 26 Caress, D. W. *et al.* Repeat bathymetric surveys at 1-metre resolution of lava flows erupted at Axial Seamount in April 2011. *Nature Geosci* **5**, 483-488, doi:10.1038/ngeo1496 (2012).

- 27 Clague, D. A. *et al.* High-resolution AUV mapping and targeted ROV observations of three historical  
 28 lava flows at Axial Seamount. *Oceanography* **30**, 82-99 (2017).
- 29 Bachelery, P. *et al.* Petrological and Geochemical Characterization of the Lava from the 2018-2019  
 30 Mayotte Eruption: First Results. *AGUFM* **2019**, V52D-06 (2019).
- 31 Cathalot, C. *et al.* Acoustic and Geochemical Anomalies in the Water Column around the Newly  
 32 Formed Volcano offshore Mayotte Island. *AGUFM* **2019**, V52D-05 (2019).
- 33 Resing, J. A. *et al.* Active submarine eruption of boninite in the northeastern Lau Basin. *Nature*  
 34 *Geoscience* **4**, 799-806 (2011).
- 35 Baumberger, T. *et al.* Understanding a submarine eruption through time series hydrothermal plume  
 36 sampling of dissolved and particulate constituents: West Mata, 2008–2012. *Geochemistry,*  
 37 *Geophysics, Geosystems* **15**, 4631-4650 (2014).
- 38 Baker, E. T. *et al.* Hydrothermal discharge during submarine eruptions: The importance of detection,  
 39 response, and new technology. *Oceanography* **25**, 128-141 (2012).
- 40 Chadwick, W. W. *et al.* Imaging of CO<sub>2</sub> bubble plumes above an erupting submarine volcano, NW  
 41 Rota - 1, Mariana Arc. *Geochemistry, Geophysics, Geosystems* **15**, 4325-4342 (2014).
- 42 Somoza, L. *et al.* Evolution of submarine eruptive activity during the 2011–2012 El Hierro event as  
 43 documented by hydroacoustic images and remotely operated vehicle observations. *Geochemistry,*  
 44 *Geophysics, Geosystems* **18**, 3109-3137 (2017).
- 45 Sohn, R. A. *et al.* Explosive volcanism on the ultraslow-spreading Gakkel ridge, Arctic Ocean. *Nature*  
 46 **453**, 1236-1238 (2008).
- 47 Barreyre, T., Soule, S. A. & Sohn, R. A. Dispersal of volcanoclasts during deep-sea eruptions: Settling  
 48 velocities and entrainment in buoyant seawater plumes. *Journal of Volcanology and Geothermal*  
 49 *Research* **205**, 84-93 (2011).
- 50 Tarantola, A. Linearized inversion of seismic reflection data. *Geophysical prospecting* **32**, 998-1015  
 51 (1984).
- 52 Anderson, E. Dynamics of formation of cone-sheets, ring-dikes, and cauldron subsidences: Royal  
 53 Society of Edinburgh Proceedings, v. 56. (1936).
- 54 Nikkhoo, M., Walter, T. R., Lundgren, P. R. & Prats-Iraola, P. Compound dislocation models (CDMs)  
 55 for volcano deformation analyses. *Geophysical Journal International*, ggw427 (2016).
- 56 Dofal, A., Fontaine, F. R., Michon, L., Barruol, G. & Tkalcic, H. in *AGU Fall Meeting 2018*. (AGU).  
 57 Wolfe, C. J., Okubo, P. G. & Shearer, P. M. Mantle fault zone beneath Kilauea volcano, Hawaii.  
 58 *Science* **300**, 478-480 (2003).
- 59 Wright, T. L. & Klein, F. W. Deep magma transport at Kilauea volcano, Hawaii. *Lithos* **87**, 50-79,  
 60 doi:10.1016/j.lithos.2005.05.004 (2006).
- 61 Merz, D., Caplan - Auerbach, J. & Thurber, C. Seismicity and Velocity Structure of Lō'ihi Submarine  
 62 Volcano and Southeastern Hawai'i. *Journal of Geophysical Research: Solid Earth* **124**, 11380-11393  
 63 (2019).
- 64 Michon, L., Ferrazzini, V., Di Muro, A., Villeneuve, N. & Famin, V. Rift zones and magma plumbing  
 65 system of Piton de la Fournaise volcano: How do they differ from Hawaii and Etna. *J. Volc. Geotherm.*  
 66 *Res.* **303**, 112-129, doi:10.1016/j.jvolgeores.2015.07.031 (2015).
- 67 Cesca, S. *et al.* Very long period signals and seismic swarm activity offshore Mayotte, Comoro Islands.  
 68 (2019).
- 69 Toda, S., Stein, R. & Sagiya, T. Evidence from the AD 2000 Izu islands earthquake swarm that  
 70 stressing rate governs seismicity. *Nature* **419**, 58-61, doi:10.1038/nature00997 (2002).
- 71 Hayashi, Y. & Morita, Y. An image of a magma intrusion process inferred from precise hypocentral  
 72 migrations of the earthquake swarm east of the Izu Peninsula. *Geophysical Journal International* **153**,  
 73 159-174 (2003).
- 74 Ágústsdóttir, T. *et al.* Strike - slip faulting during the 2014 Bárðarbunga - Holuhraun dike intrusion,  
 75 central Iceland. *Geophysical Research Letters* **43**, 1495-1503 (2016).
- 76 Ukawa, M. & Tsukahara, H. Earthquake swarms and dike intrusions off the east coast of Izu Peninsula,  
 77 central Japan. *Tectonophysics* **253**, 285-303 (1996).
- 78 Sigmundsson, F. *et al.* Segmented lateral dyke growth in a rifting event at Bárðarbunga volcanic  
 79 system, Iceland. *Nature* **517**, 191-195, doi:10.1038/nature14111 (2015).
- 80 Jacques, E. *et al.* in *AGU* (Online everywhere, 2020).
- 81 Filson, J., Simkin, T. & Leu, L. k. Seismicity of a caldera collapse: Galapagos Islands 1968. *Journal of*  
 82 *Geophysical Research* **78**, 8591-8622 (1973).
- 83 Geshi, N. & Oikawa, T. Phreatomagmatic eruptions associated with the caldera collapse during the  
 84 Miyakejima 2000 eruption, Japan. *Journal of volcanology and geothermal research* **176**, 457-468  
 85 (2008).

- 54 Gudmundsson, M. T. *et al.* Gradual caldera collapse at Bárðarbunga volcano, Iceland, regulated by lateral magma outflow. *Science* **353**, aaf8988 (2016).
- 55 Roche, O., Druitt, T. & Merle, O. Experimental study of caldera formation. *Journal of Geophysical Research: Solid Earth* **105**, 395-416 (2000).
- 56 Kumagai, H. & Chouet, B. A. Acoustic properties of a crack containing magmatic or hydrothermal fluids. *Journal of Geophysical Research: Solid Earth* **105**, 25493-25512 (2000).
- 57 Woods, J. *et al.* Long-period seismicity reveals magma pathways above a laterally propagating dyke during the 2014–15 Bárðarbunga rifting event, Iceland. *Earth and planetary science letters* **490**, 216-229 (2018).
- 58 Kumagai, H. *et al.* Magmatic dike resonances inferred from very-long-period seismic signals. *Science* **299**, 2058-2061 (2003).
- 59 Kobayashi, T., Ohminato, T., Ida, Y. & Fujita, E. Very long period seismic signals observed before the caldera formation with the 2000 Miyake - jima volcanic activity, Japan. *Journal of Geophysical Research: Solid Earth* **114** (2009).
- 60 Aster, R. *et al.* Very long period oscillations of Mount Erebus Volcano. *Journal of Geophysical Research: Solid Earth* **108** (2003).
- 61 Shuler, A. & Ekström, G. Anomalous earthquakes associated with Nyiragongo Volcano: Observations and potential mechanisms. *Journal of Volcanology and Geothermal Research* **181**, 219-230 (2009).
- 62 Fazio, M., Alparone, S., Benson, P. M., Cannata, A. & Vinciguerra, S. Genesis and mechanisms controlling tornillo seismo-volcanic events in volcanic areas. *Scientific reports* **9**, 1-11 (2019).
- 63 Maeda, Y. & Kumagai, H. A generalized equation for the resonance frequencies of a fluid-filled crack. *Geophysical Journal International* **209**, 192-201 (2017).
- 64 Kumagai, H. *et al.* Very-Long-Period Seismic Signals and Caldera Formation at Miyake Island, Japan. *Science* **293**, 687-690, doi:10.1126/science.1062136 (2001).
- 65 Sigmundsson, F. *et al.* Unexpected large eruptions from buoyant magma bodies within viscoelastic crust. *Nature Communications* **11**, 1-11 (2020).
- 66 Bachèlery, P. *et al.* in *Active Volcanoes of the Southwest Indian Ocean* 345-366 (Springer, 2016).
- 67 Armijo, R., Meyer, B., Navarro, S., King, G. & Barka, A. Asymmetric slip partitioning in the Sea of Marmara pull - apart: A clue to propagation processes of the North Anatolian fault? *Terra Nova* **14**, 80-86 (2002).
- 68 Dauteuil, O. & Brun, J.-P. Oblique rifting in a slow-spreading ridge. *Nature* **361**, 145-148 (1993).
- 69 Brune, S. Evolution of stress and fault patterns in oblique rift systems: 3 - D numerical lithospheric - scale experiments from rift to breakup. *Geochemistry, Geophysics, Geosystems* **15**, 3392-3415 (2014).
- 70 Corti, G. Evolution and characteristics of continental rifting: Analog modeling-inspired view and comparison with examples from the East African Rift System. *Tectonophysics* **522**, 1-33 (2012).
- 71 Pagli, C., Yun, S.-H., Ebinger, C., Keir, D. & Wang, H. Strike-slip tectonics during rift linkage. *Geology* **47**, 31-34 (2019).
- 72 Franke, D. *et al.* The offshore East African Rift System: Structural framework at the toe of a juvenile rift. *Tectonics* **34**, 2086-2104 (2015).
- 73 Rufer, D., Preusser, F., Schreurs, G., Gnos, E. & Berger, A. Late Quaternary history of the Vakinankaratra volcanic field (central Madagascar): insights from luminescence dating of phreatomagmatic eruption deposits. *Bulletin of volcanology* **76**, 817 (2014).
- 74 Kusky, T. M., Toraman, E., Raharimahefa, T. & Rasoazanamparany, C. Active tectonics of the Alaotra–Ankay Graben System, Madagascar: possible extension of Somalian–African diffuse plate boundary? *Gondwana Research* **18**, 274-294 (2010).
- 75 Peacock, D. & Anderson, M. THE SCALING OF PULL - APARTS AND IMPLICATIONS FOR FLUID FLOW IN AREAS WITH STRIKE - SLIP FAULTS. *Journal of Petroleum Geology* **35**, 389-399 (2012).
- 76 Pratt, M. J. *et al.* Shear velocity structure of the crust and upper mantle of Madagascar derived from surface wave tomography. *Earth and Planetary Science Letters* **458**, 405-417 (2017).
- 77 Mazzullo, A. *et al.* Anisotropic Tomography Around La Réunion Island From Rayleigh Waves. *J. Geophys. Res. Solid Earth* **122**, 9132-9148, doi:10.1002/2017JB014354 (2017).
- 78 Barruol, G. *et al.* Large-scale flow of Indian Ocean asthenosphere driven by Réunion plume. *Nat. Geosci.* **12**, 1043-1049, doi:10.1038/s41561-019-0479-3 (2019).
- 79 Zhong, S. & Watts, A. Lithospheric deformation induced by loading of the Hawaiian Islands and its implications for mantle rheology. *Journal of Geophysical Research: Solid Earth* **118**, 6025-6048 (2013).
- 80 Watts, A. B. *et al.* Rapid rates of growth and collapse of Monowai submarine volcano in the Kermadec Arc. *Nature Geosci* **5**, 510-515, doi:10.1038/ngeo1473 (2012).

- 81 Chadwick Jr, W. W. *et al.* A recent volcanic eruption discovered on the central Mariana back-arc  
spreading center. *Frontiers in Earth Science* **6**, 172 (2018).
- 82 Schipper, C. I., White, J. D., Houghton, B., Shimizu, N. & Stewart, R. B. Explosive submarine  
eruptions driven by volatile-coupled degassing at Lōihi Seamount, Hawaii. *Earth and Planetary  
Science Letters* **295**, 497-510 (2010).
- 83 Carey, R. J., Wysoczanski, R., Wunderman, R. & Jutzeler, M. Discovery of the largest historic silicic  
submarine eruption. *Eos, Transactions American Geophysical Union* **95**, 157-159 (2014).
- 84 Carey, R. *et al.* The largest deep-ocean silicic volcanic eruption of the past century. *Science advances* **4**,  
e1701121 (2018).
- 85 Bonny, E., Thordarson, T., Wright, R., Höskuldsson, A. & Jónsdóttir, I. The volume of lava erupted  
during the 2014 to 2015 eruption at Holuhraun, Iceland: A comparison between satellite - and  
ground - based measurements. *Journal of Geophysical Research: Solid Earth* **123**, 5412-5426 (2018).
- 86 Thordarson, T. & Self, S. The Laki (Skaftár Fires) and Grímsvötn eruptions in 1783-1785 *Bull Volcanol*  
**55**, 233-263 (1993).
- 87 Neal, C. *et al.* The 2018 rift eruption and summit collapse of Kīlauea Volcano. *Science* **363**, 367-374  
(2019).
- 88 Cogné, J.-P. & Humler, E. Temporal variation of oceanic spreading and crustal production rates during  
the last 180 My. *Earth and Planetary Science Letters* **227**, 427-439 (2004).
- 89 Marty, B. & Tolstikhin, I. N. CO<sub>2</sub> fluxes from mid-ocean ridges, arcs and plumes. *Chemical Geology*  
**145**, 233-248 (1998).
- 90 REVOSIMA, R. d. s. V. e. S. d. M. Bulletin n°16 de l'activité sismo-volcanique à Mayotte, du 1 au 31  
mars 2020. (2020).
- 91 Globe (GLobal Oceanographic Bathymetry Explorer) Software. (2020).
- 92 Lomax, A., Michelini, A. & Curtis, A. Earthquake location, direct, global-search methods.  
*Encyclopedia of complexity and system science* **5**, 1-33 (2009).
- 93 Poiata, N., Satriano, C., Vilotte, J.-P., Bernard, P. & Obara, K. Multiband array detection and location  
of seismic sources recorded by dense seismic networks. *Geophysical Journal International* **205**, 1548-  
1573 (2016).
- 94 SHOM. (MNT\_MAY100m\_HOMONIM\_WGS84, 2016).
- 95 JORRY, S. (2014).
- 96 Debeuf, D. *Étude de l'évolution volcano-structurale et magmatique de Mayotte, Archipel des Comores,  
océan Indien: approches structurale, pétrographique, géochimique et géochronologique*, (2009).
- 97 Ekström, G., Nettles, M. & Dziewoński, A. The global CMT project 2004–2010: Centroid-moment  
tensors for 13,017 earthquakes. *Physics of the Earth and Planetary Interiors* **200**, 1-9 (2012).
- 98 Stamps, D., Saria, E. & Kreemer, C. A Geodetic Strain Rate Model for the East African Rift System.  
*Sci, Rep*, **8**, 732, doi:10.1038/s41598-017-19097-w (2018).
- 99 Mougenot, D., Hernandez, J. & Virlogeux, P. Structure et volcanisme d'un rift sous-marin; le fosse des  
Kerimbias (marge nord-mozambique). *Bulletin de la Société Géologique de France*, 401-410 (1989).
- 100 Deville, E. *et al.* Active fault system across the oceanic lithosphere of the Mozambique Channel:  
implications for the Nubia–Somalia southern plate boundary. *Earth and Planetary Science Letters* **502**,  
210-220 (2018).
- 101 Macgregor, D. History of the development of the East African Rift System: A series of interpreted maps  
through time. *Journal of African Earth Sciences* **101**, 232-252 (2015).

## FIGURE CAPTIONS

**Figure 1:** The volcanic ridge offshore Mayotte. a) Westward view of Mayotte island and insular slope (vertical exaggeration 3) with MAYOBS1 cruise multibeam EM122 bathymetry (resolution: 30m<sup>18</sup>) superimposed on a previous bathymetry-topography compilation<sup>16,94</sup>. The volcanic Mayotte ridge extends from the onshore Mamoudzou-Petite Terre volcanic zones to the new volcanic edifice (NVE). Green arrows and stars: location of acoustically-detected plumes above the Horseshoe, the NVE and the degassing area on Petite-Terre island. Left inset: geographic setting and surface horizontal displacements (with plate velocity removed) recorded by Global Navigation Satellite System (GNSS) stations in Mayotte, Grande Glorieuse and Madagascar (Diego Suarez). Black points: seismic stations (details and name in Supplementary material). Dashed grey lines: NNW-SSE to N-S striking Mesozoic fracture zones resulting from the Gondwana break-up<sup>6</sup>. b) MAYOBS1 multibeam bathymetry superimposed over slopes (dark zones: steep slopes) and geological interpretations. Volcanic structures are indicated in purple (mainly cones) and pink (lava flows and elongated features). In yellow: Upper slope's highly reflective patches (backscatter data). The NVE is indicated in red (central part with steep slopes) and orange (radial ridges and flat flows). Green stars: degassing areas detected acoustically (on the Horseshoe) and visually (on Petite-Terre)<sup>17</sup>. Red lines: fissures and faults, dashed lines for inferred faults. Area filled with small black dots: bathymetric depression. White boxes: location of Fig.2a and Extended data Fig. 3. Inset, as in b with Mayotte ridge segments underlined by red and purple colored patches, pink dots: seismicity recorded during the Ocean Bottom seismometer (OBS) deployment and relocated on board; yellow diamonds: location of the Very Low Frequency earthquakes c) MAYOBS1 multibeam backscatter map (white = higher reflectivity). Shallow bathymetry and topography are the same as in a). Pink dots and yellow diamonds as in b) inset. Black and white boxes: location of extended data Figure 3, respectively.

**Figure 2: The new volcanic edifice (NVE) offshore Mayotte.** a) 30 m resolution bathymetric maps from shipboard EM122 multibeam, illuminated from N290°E. Left panel: SHOM bathymetry collected in 2014<sup>19</sup>. Right panel: MAYOBS1 bathymetry collected in May 2019<sup>18</sup>. Red circle: position of dredge DR01. b) Depth changes between 2014 and 2019. The change in topography is estimated to be significant when larger than 10 m.

**Figure 3:** a) Southward 3D view of the NVE and the water column acoustic plume observed one hour before the Conductivity-Temperature-Depth (CTD) rosette on May 16th 2019 (White dot and blue patch) deployed, 1 km far from the summit the volcano (*see Extended data Figure 4*). Right inset: Processed polar echogram from one EM122 multibeam ping on May 16th (13:33 UT), horizontal and vertical-axes (both in meters) correspond respectively to the cross-track distance and the water depth. See also Acoustic plume movie 1.

**Figure 4: Conceptual model of the submarine eruption offshore Mayotte eruption:** Bathymetry as in Figure 1b, no vertical exaggeration. Red zones on the seafloor: N130°E volcano-tectonic ridges (Jumelles ridges) and segments including Mayotte ridge eastern segment. Dashed white lines: inferred ancient caldera with degassing zones above. In cross-section: red and reddish zones: magma storage zones (mush or magma chambers) and magma pathways involved in the 2018-2020 Mayotte volcanic crisis and seafloor eruption. Yellow layer: sediments. Dashed lines: subvertical faults beneath inferred caldera possibly reactivated by the deflation of a deep reservoir. White arrow: possible downsag at an initial stage of caldera collapse. Pink dots: 800 earthquakes between 25 February and May 6 2019 located using OBSs and land stations. Other dots: 139 earthquakes from before the OBS deployment, picked on land stations and relocated using a new model based on the OBS+land data: colored dots are from the first 6 weeks of the crisis and white dots from the remaining 8 months before the OBS deployment. Yellow diamonds: Very Low Frequency (VLF) earthquakes, constrained by the OBS+land network. Blue and red triangles: water and magma movements, respectively. Blue patch: Location, with 3 sigma uncertainties, of the most robust isotropic source deformation model. Moho depth from <sup>40</sup>. Lithosphere/asthenosphere boundary depth from <sup>77,78</sup>.

**Figure 5: Regional volcano-tectonic setting of the submarine eruption offshore Mayotte.**  
a) Volcano-tectonic setting of the new volcanic edifice (NVE). Bathymetry compiled from MAYOBS1 cruise <sup>18</sup>, PTOLEMEE Cruise <sup>95</sup>, and the General Bathymetric Chart of the Oceans (<https://www.gebco.net>). Global topography from SRTM GL1

(<https://catalog.data.gov/dataset/shuttle-radar-topography-mission-srtm-g11-global-30m>).

Volcanic cones and ridges (purple) from <sup>13,96,16,14</sup> and this study. Dots and diamonds are earthquakes as in Figure 4 and Extended data Fig. 6 and 8. Beach balls: focal mechanisms for  $M > 5$  earthquakes <sup>97</sup>. Dotted white arrow: dyking event along the  $N130^\circ E$  trending eastern segment of the Mayotte volcanic ridge. Red ellipse: inferred main volcano-tectonic ridges (Mayotte, Jumelles...). Purple ellipses: highly damaged zones in between the en echelon ridges (see sandbox model in Inset). Thick black arrows: local extension direction. Inset: sandbox model from <sup>75</sup> illustrating the possible arrangement of the main volcano-tectonic structures in Comoros (see also Extended data Figure 9). b) Geodynamic setting of the East African Rift systems. Bathymetry from GeoMapApp ([www.geomapapp.org](http://www.geomapapp.org)), main tectonic structures and extensional zones in Africa and Madagascar adapted from <sup>98,73,74,99,100,101,72</sup> and references therein. Purple patches: Quaternary volcanism in Madagascar from <sup>73</sup>. Red dots:  $M > 2.5$  earthquakes <sup>4</sup> with focal mechanisms from the Global Centroid-Moment-Tensor Project <sup>97</sup> for the  $M > 5$  earthquakes. Arrows: GNSS horizontal motions <sup>98</sup>. Small purple ellipses in the Comoros as in a) with double dark red arrows: the volcanic ridge east of Mayotte and extension direction. Inset: Simplified tectonic map of the East African Rift system: Yellow highlights: most active rifts and grabens; Red ellipse: Transfer zone of the Comoros with direction of lateral motion.

**Extended data. Figure 1:** 3-D westward view of submarine volcanic features located east of Mayotte, 3x vertical exaggeration. Bathymetry from MAYOBS1 30-m resolution DTM and previous bathymetry-topography compilation <sup>16,94</sup> a) bathymetry (b) Backscatter seafloor reflectivity (white is highest reflectivity) from MAYOBS1 cruise.

**Extended data. Figure 2:** Volcanic features offshore Mayotte. a) 30-m resolution EM122 multibeam bathymetry (MAYOBS 1 cruise) superimposed on a previous bathymetry-topography compilation <sup>16,94</sup> with locations of Fig2.b,c,d indicated. b), c) Interpreted MAYOBS1 shipboard bathymetry and backscatter of the upper slope east of Mayotte (location in a). Cones, lava flows and canyons as in Figure 1b. Black dots: bathymetric depression. Dashed red lines: possible pre-existing caldera structure. d) Interpreted bathymetry of the lower slope east of Mayotte (localisation in a). e) zoom on d) showing monogenetic cones and lava flows

**Extended data. Figure 3:** New volcanic edifice. a) 2014 EM122 multibeam seafloor backscatter <sup>19</sup>. b) 2019 reflectivity (MAYOBS 1 cruise) <sup>18</sup>. c) Depth changes between the 2014 and 2019 surveys, superimposed on 2019 reflectivity. The white areas of the 2019 backscatter map exceeding the bathymetric difference map indicate the extent of new volcanic material.

**Extended data. Figure 4:** CTD (conductivity temperature-depth)-Rosette measurements. a) Nephelometry and b) temperature vertical profiles. c)-g) sample analyses from 8L @Niskin bottles. c)-e) Gas concentrations(CH<sub>4</sub>, H<sub>2</sub>, CO<sub>2</sub>); .f) pH, g) total alkalinity and total CO<sub>2</sub>.

**Extended data. Figure 5:** Acoustic plumes over the Horseshoe volcanic structure. a) Southward 3D view of the horseshoe morphology and two water column acoustic plumes observed on the western internal flank. b) Processed polar echogram from one EM122 multibeam ping of the data set displayed in (a) acquired on May 18th (0541 UT) horizontal and vertical-axes correspond respectively to the cross-track distance and the water depth, in meters) – see also Acoustic plume movie 2.

**Extended data. Figure 6:** Top: map views, bottom: cross-sections (A-A') projection along azimuth N115°E; (B-B') along azimuth N45°E. a) Earthquakes recorded by onshore seismological stations before the deployment of the Ocean bottom seismometers (OBS). Colored circles are events occurring in the first six weeks of the crisis, white circles are earthquakes in the intervening 8 months. b) Earthquakes recorded by the OBS+land stations between February 25 and May 6 2019 (pink dots). Yellow diamonds: location of the Very Low Frequency (VLF) events located in this study (see supplementary information). c) Focal mechanisms of the largest earthquakes from the Harvard CMT catalog (<https://www.globalcmt.org/>), with color scale as in a).

**Extended data. Figure 7** - Global Navigation Satellite System (GNSS) data modelling and seafloor subsidence estimated from seafloor pressure variations. a) Map shows the locations of the stations used. Arrows with colors with names: GNSS velocity vectors (mm/yr) and station names. Coloured numbers: vertical deformation (mm/yr). Inset: yellow dots locate pressure sensors on ocean bottom seismometer stations (see Fig.S2.1 for names), red arrows: Mayotte GNSS velocity vectors (mm/yr), white arrows: far field GNSS velocity vectors. b) GNSS Time series with relative displacements recorded on the east (top), north (middle) and vertical (bottom) components of the stations between January 2018 and January 2020. c) Best fit-models with  $1\sigma$  uncertainties of the GNSS data for one isotropic point source and a triple volumetric discontinuity pCDM source. d) Top panel: Pressure recorded by Seabird SBE37 gauges at the six ocean-bottom seismometer stations (Yellow dots inset Figure 7a and Fig. S2.1) de-tided and converted to vertical motion. Middle panel: vertical deformation estimated at each seafloor instrument location, using the best isotropic source model obtained from the GNSS data for the March 1st to May 1st 2019 period. Lower panel: residual signal after subtracting the model-predicted trend from the seafloor pressure variations. This residual probably contains instrumental drift (especially in the first 2 weeks of the deployment) but may also include some mis-modelled seafloor deformation. The residuals at stations MOSE and MONE (see location on Figure S2.1) exhibit slight negative and positive trends, respectively which could indicate that the volcanic source is located a bit further south than that modelled using the GNSS data, assuming that instrumental drift is not the dominant factor.

**Extended data. Figure 8:** Conceptual model for the Mayotte seismo-volcanic event. Circles and diamonds are events as in Extended data - Figure 6. Focal mechanisms of main earthquakes are from Harvard CMT catalog (<https://www.globalcmt.org/><sup>97</sup>) with the same color scale as the May 10 to June 30, 2018 events, Yellow circle and blue patch: Location, with 3 sigma uncertainties, of the most robust isotropic source deformation model. a) Map view: The redish ellipse: Mayotte ridge, dashed circular area: old caldera structure in the morphology b) Cross-section (projection along azimuth 115 degree). Symbols as in a). Red lines: magma migration (dykes). Red ellipses and circle: magma reservoirs or mushes. Pink arrow: possible downsag along caldera structures. Redish zone: Eastern segment of the Mayotte ridge.

**Extended data. Figure 9: Regional volcano-tectonic setting of the submarine eruption offshore Mayotte.** a) Volcano-tectonic setting of the new volcanic edifice (NVE). Bathymetry compiled from MAYOBS1 cruise<sup>18</sup>, PTOLEMEE cruise<sup>95</sup>, and the General Bathymetric Chart of the Oceans (<https://www.gebco.net>). Global topography from SRTM GL1 (<https://catalog.data.gov/dataset/shuttle-radar-topography-mission-srtm-gl1-global-30m>). Volcanic cones and ridges (purple) from<sup>13,96,16,14</sup> and this study. Beach balls: focal mechanisms for M>5 earthquakes<sup>97</sup>. Dotted white arrow: dyking event along the N130° E trending eastern segment of the volcanic ridge. Pink ellipse: inferred main volcano-tectonic ridges. Purple ellipses: highly damaged zones in between the en-echelon ridges (see sand box model Inset of Figure 5). Thick black arrows: local extension direction.

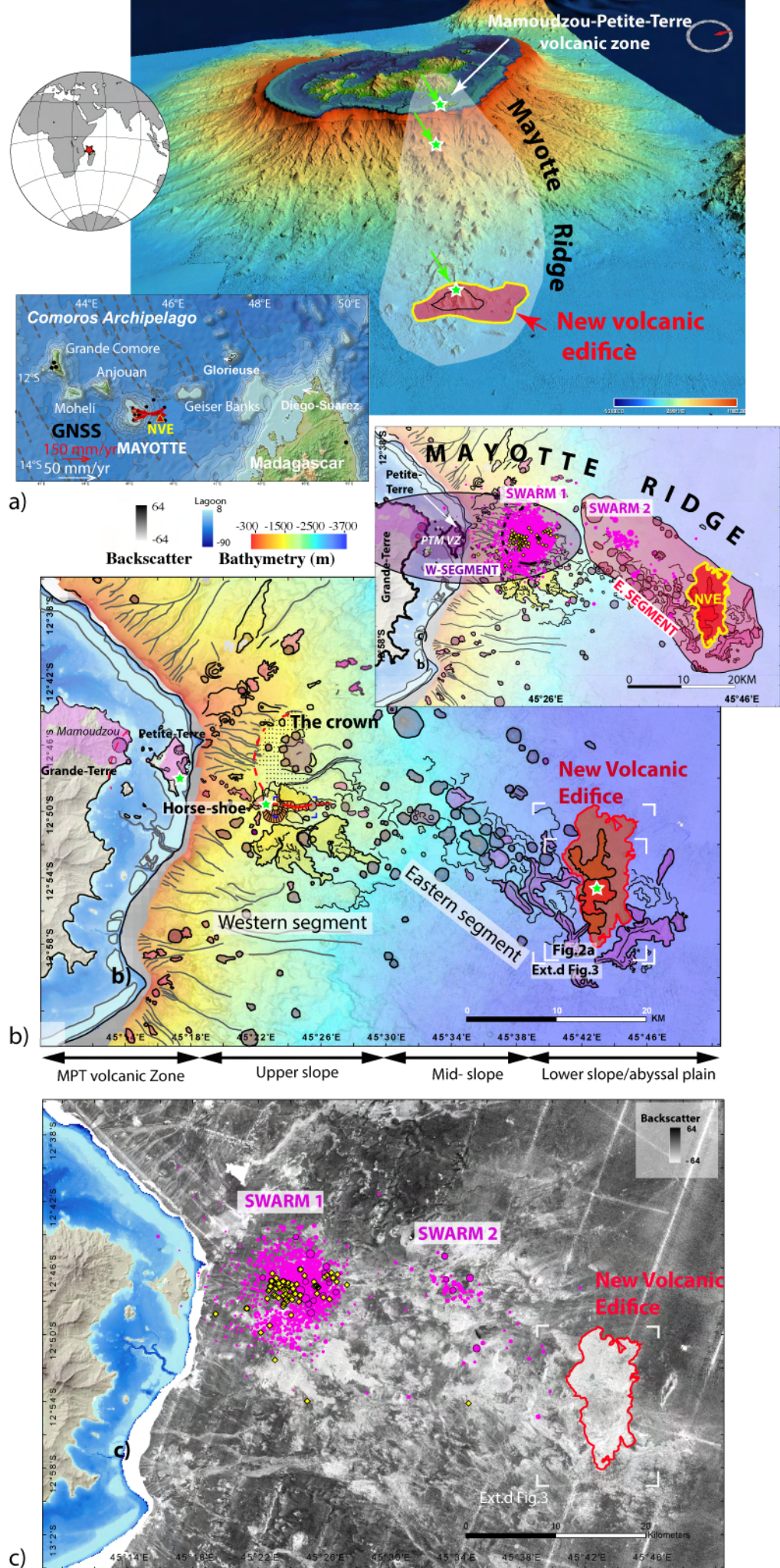
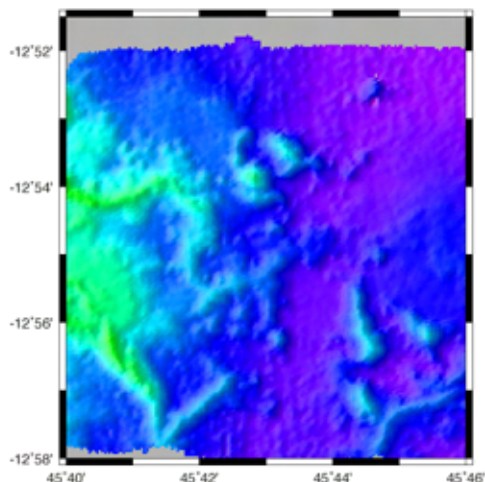
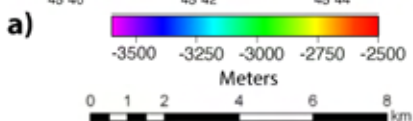
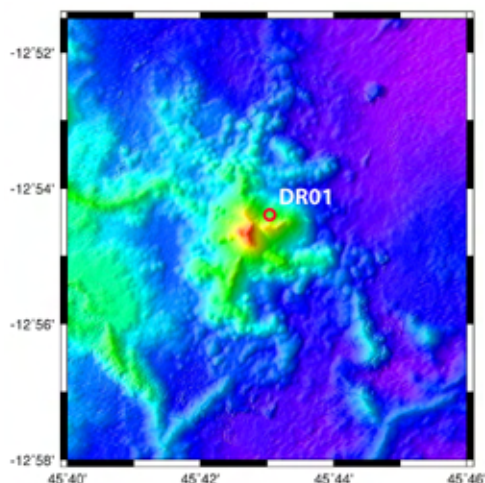


**Figure 1**

# SHOM 2014



# MAYOBS1 2019



# Difference 2014-2019

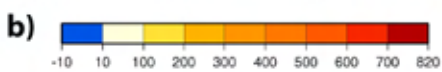
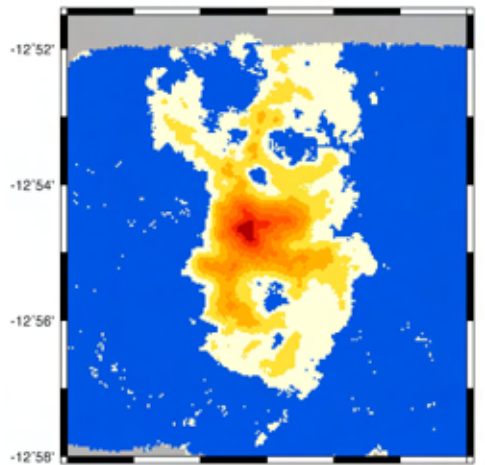
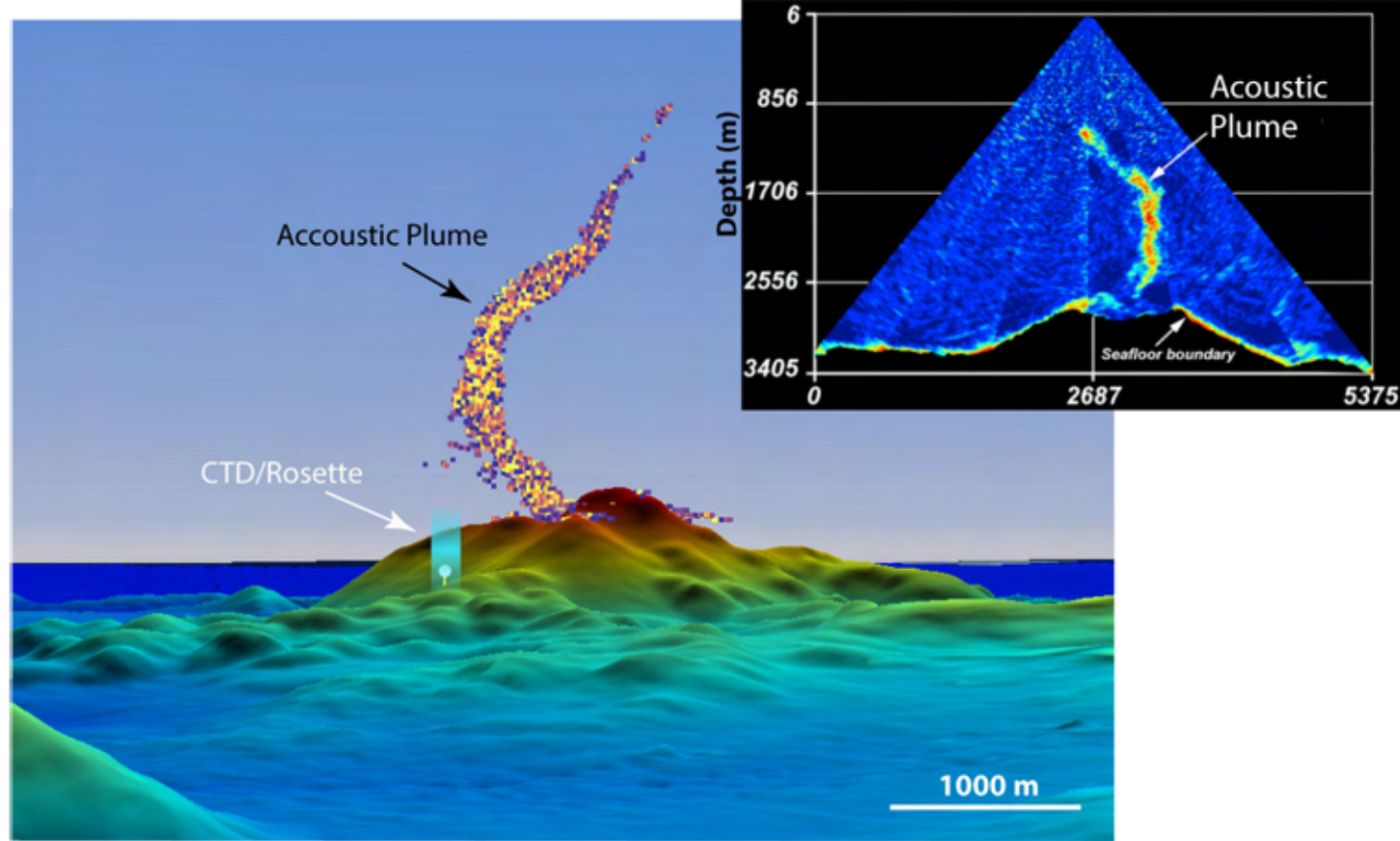
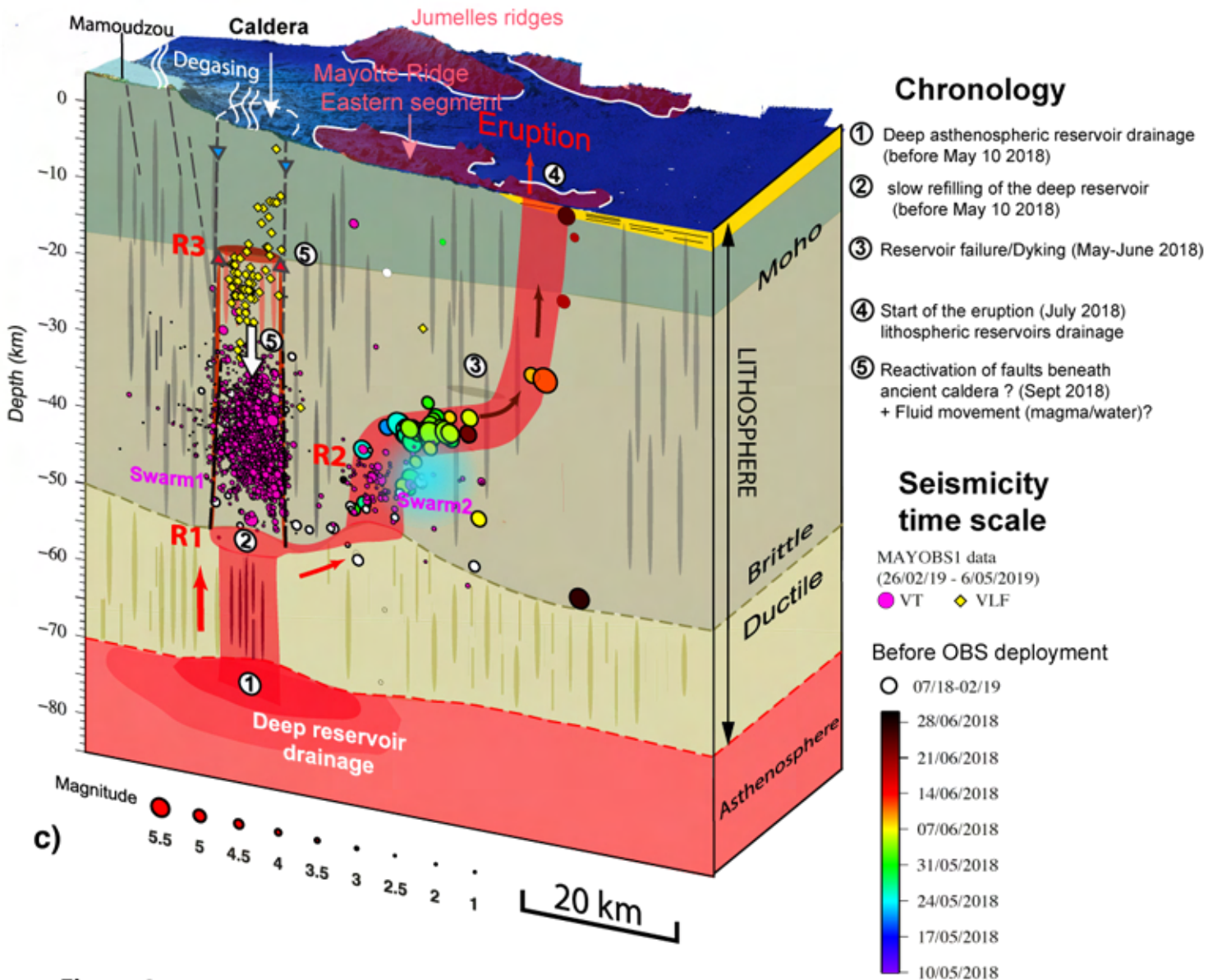


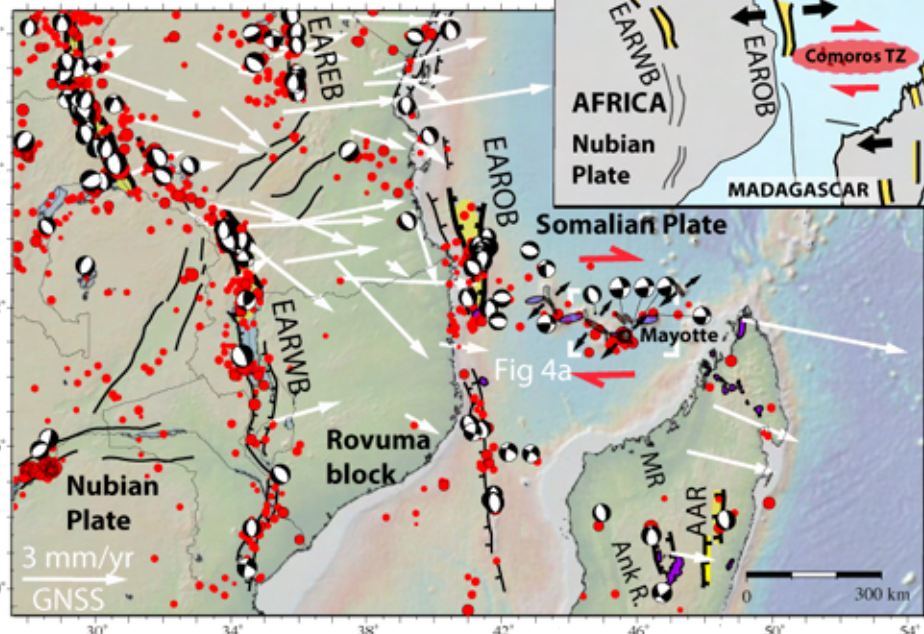
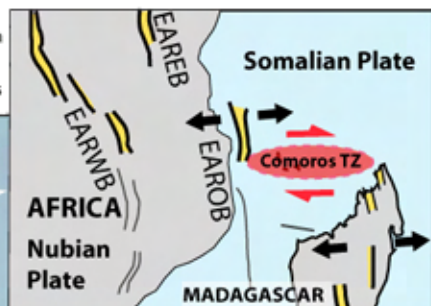
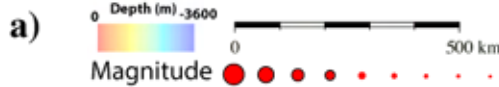
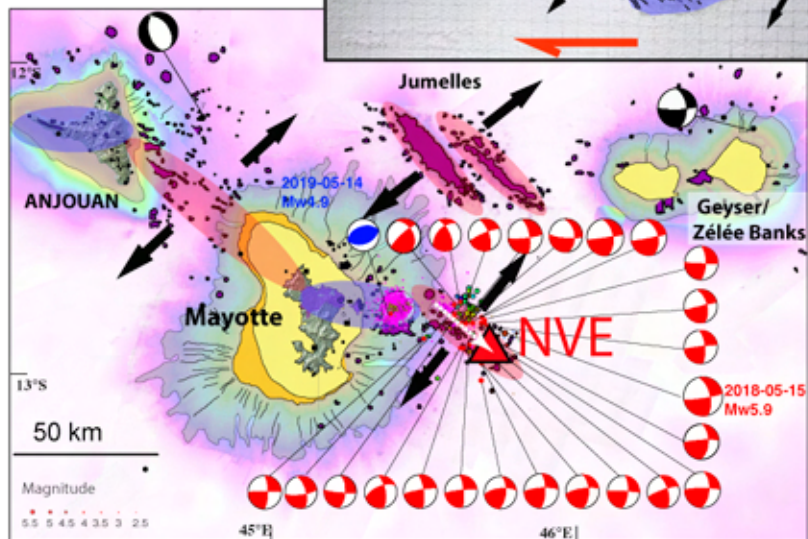
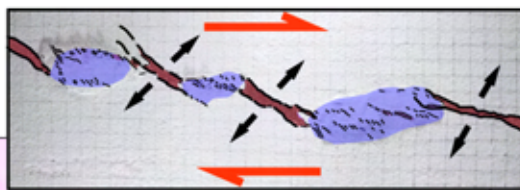
Figure 2



c)

Figure 3





b)

Figure 5